J. Fluid Mech. (1987), *vol.* 178, *pp.* 137–159
Printed in Great Britain

Axisymmetrization and vorticity-gradient intensification of an isolated two-dimensional vortex through filamentation

By M. V. MELANDER†, J. C. McWILLIAMS AND N. J. ZABUSKY†

National Center for Atmospheric Research, PO Box 3000, Boulder, CO 80307, USA

(Received 9 September 1985 and in revised form 11 June 1986)

We consider the evolution of an isolated elliptical vortex in a weakly dissipative fluid. It is shown computationally that a spatially smooth vortex relaxes inviscidly towards axisymmetry on a circulation timescale as the result of filament generation. Heuristically, we derive a simple geometrical formula relating the rate of change of the aspect ratio of a particular vorticity contour to its orientation relative to the streamlines (where the orientation is defined through second-order moments). Computational evidence obtained with diagnostic algorithms validates the formula. By considering streamlines in a corotating frame and applying the new formula, we obtain a detailed kinematic understanding of the vortex's decay to its final state through a primary and a secondary breaking. The circulation transported into the filaments although a small fraction of the total, breaks the symmetry and is the chief cause of axisymmetrization.

1. Introduction

In the last decade there have been numerous numerical studies of freely evolving and forced nearly inviscid hydrodynamic flows in two dimensions. McWilliams (1984) showed that unforced flows and initially power-law spectra with random phases rapidly evolved into many isolated vortex regions with non-Gaussian statistics. Yet there is virtually no real understanding of two processes that play an essential role in the long-time evolution of turbulent-like states, namely the evolution towards axisymmetry of isolated, initially non-axisymmetric states and the merger of pairs of isolated vorticity regions. In a series of four papers we will clarify these processes by carefully analysing high-resolution simulations (up to 256^2) with a pseudospectral code.

In this first paper we examine the evolution of isolated spatially smooth elliptical vorticity distributions (or elliptical vortices for short). The choice of the elliptical shape is motivated by a number of mathematical and physical facts. The elliptical uniform (tophat) vortex (Kirchhoff's elliptical vortex) is a steady-state solution of the Euler equations (Lamb 1932). Hernan & Jimenez (1982) applied image-processing methods and found that near-elliptical vorticity distributions evolve and merge in laboratory experiments with free shear layers. Furthermore, a uniform vorticity distribution maintains an elliptical shape in simple time-varying strain fields (Kida 1981). The elliptical vorticity distribution also provides mathe-

† Present address: Institute for Computational Mathematics and Applications, Department of Mathematics and Statistics, University of Pittsburgh, Pittsburgh, PA 15260, USA.

matically convenient approximations. Also, we find that our results apply to near-elliptical vortices as well. Since Kirchhoff's ellipse is linearly stable for aspect ratios less than three, one might expect corresponding smooth vorticity distributions to be near-steady states evolving slowly towards axisymmetry as a result of weak dissipation. However, our essential conclusion is that there is an inviscid trend towards axisymmetry occurring during the first half revolution of the vortex. It occurs as a consequence of the generation of vortex filaments which break the elliptical symmetry. This process can be motivated easily by comparing the vorticity and a corotating stream function.

The second paper will deal with the symmetric merger of two identical vorticity regions. We show that merger, when it occurs, results from a similar axisymmetrization process caused by the same mechanism as for a single vortex. However, the merger process causes a much stronger enstrophy cascade. Furthermore, we have obtained a vital clarification of the causes and conditions for merger by comparing results from a Hamiltonian moment model (Melander, Styczek & Zabusky 1984; Melander, Zabusky & Styczek 1986) with pseudospectral calculations. The former is an integrable system for two identical vortex regions. Computationally observed pulsating states (Zabusky, Hughes and Roberts 1979) are also explained in this context.

The third paper will be devoted to the generic merger problem, that is, the merger of two vortices of different shape, circulation, spatial extent and peak vorticity.

The last paper in the series will examine two dissipation mechanisms $\nu_2 \Delta$ and $\nu_4 \Delta^2$, where the first yields the Navier–Stokes equations and the second is a typical 'hyperviscosity' mechanism. We conclude that the large-scale results presented in the first three papers are essentially independent of the nature of the dissipation, provided it is sufficiently weak. Actually, for finite-duration runs, the hyperviscosity code allows a higher effective Reynolds number without introducing significant spurious effects, and vorticity gradient intensification is treated better than with the Navier–Stokes code which shows stronger Gibbs-phenomena oscillations.

In §2 of the present paper, we describe the initial vorticity distribution and the algorithm and diagnostics used to study the evolutions. In §3 we present an axisymmetrization principle, governing the inviscid dynamics of the vortex. As described in §4, this principle combined with a knowledge of the corotating stream-function contours yields a detailed kinematic understanding of the relaxation towards axisymmetry. We also describe the observed gradient intensification and spiral structure in the vortex core. Section 5 deals with the dependence on the initial conditions and generalizations to geostrophic vortices ($\gamma \neq 0$ in (8)).

2. Initial vorticity distribution, algorithms and diagnostics

2.1. *Localized initial vorticity distribution*

We specify the initial vorticity distribution $\omega(r, \phi, 0)$ as an idealized smooth distribution of compact support, and with equivorticity lines that are concentric ellipses of a common orientation and aspect ratio. Outside the ellipse $r = R_0(\phi)$ there is no vorticity and inside $r = R_1(\phi)$ the vorticity is uniform $\omega = \omega_p$, see figure 1 (*a*). The relative steepness of the vorticity gradient is controlled by the parameter $\delta = [R_0 - R_1]/R_0$, (where Kirchhoff's vortex is obtained as δ tends to zero). We refer to the initial vorticity distribution as $V(\delta, \omega_p, a, b)$, where a and b are the major and minor axes of the outermost ellipse $r = R_0(\phi)$.

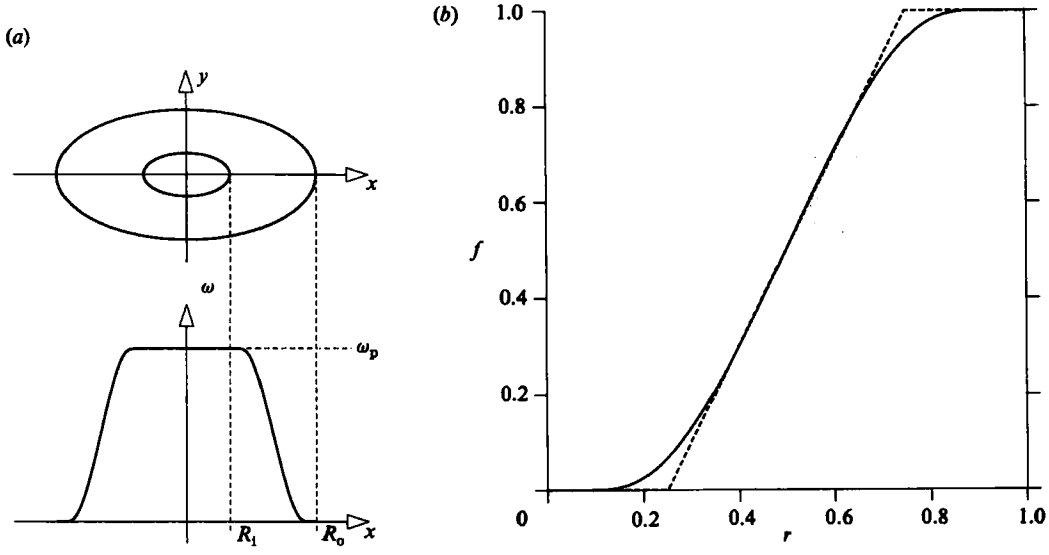

FIGURE 1. (*a*) Sketch of the initial vorticity distribution. (*b*) The profile function (2) and the piecewise linear approximation (4).

We have found it convenient to specify $\omega(r, \phi, 0)$ as a distribution with a monotonic profile function $f(r), r \geqslant 0$

$$\omega(r,\phi) = \omega_p \begin{cases} 1 & (r \leqslant R_i), \\ 1 - f[(r-R_i)/(R_o-R_i)] & (R_i < r < R_o), \\ 0 & (R_o \leqslant r). \end{cases} \tag{1}$$

We select our profile function f from the one-parameter family $\{f_\kappa; \kappa > 0\}$ where

$$f_\kappa(r) = \exp[-\kappa r^{-1} \exp(1/(r-1))], \quad 0 \leqslant r \leqslant 1. \tag{2}$$

This function smoothly connects levels 0 and 1 at $r = 0$ and $r = 1$, and all its derivatives vanish at these points. A suitable choice of κ is obtained from the natural requirement that $f(0.5) = 0.5$, this implies

$$\kappa = \tfrac{1}{2}(\exp 2)(\ln 2) \approx 2.56085. \tag{3}$$

With this value of κ we find $f'(0.5) = \ln 8 \approx 2.08$, and approximately 90% of the variation of the function f occurs within the interval $[0.25, 0.75]$ (see figure 1).

We may reasonably approximate the profile function $f_\kappa(r)$ by the piecewise linear function

$$I(r) = \begin{cases} 0, & (r \leqslant \frac{1}{4}), \\ 2r - (\frac{1}{2}), & (\frac{1}{4} \leqslant r \leqslant \frac{3}{4}), \\ 1, & (\frac{3}{4} \leqslant r). \end{cases} \tag{4}$$

This formula is useful for calculating an approximation to the total circulation of the initial vorticity distribution

$$\Gamma = \int\int \omega \, dx \, dy = \mathrm{Cir}[V(\delta, \omega_p, a, b)] = \omega_p ab \, \mathrm{Vol}[V(\delta, 1, 1, 1)], \tag{5}$$

where Vol denotes the dimensionless volume of the tophat $V(\delta, 1, 1, 1)$. Since $V(\delta, 1, 1, 1)$ is axisymmetric we find

$$\Gamma = \omega_p ab\pi \int_0^1 R(\zeta)^2 \, d\zeta,$$

where $R(\zeta)$ is the radius of the circular cross-section of $V(\delta, 1, 1, 1)$ at level ζ. This radius is found using the approximation (4), thus

$$\left.\begin{aligned} \Gamma &= \omega_p \pi ab \int_0^1 [1-\delta(\zeta+\tfrac{1}{2})/2]^2 \, d\zeta, \\ &= \omega_p \pi ab(1-\delta+(13\delta^2)/48). \end{aligned}\right\} \tag{6}$$

Hence, the parameters δ, ω_p, a and b can be easily changed subject to the constraint that Γ is maintained. The error in this approximation increases with δ. At $\delta = 1$ the error is 1.5%.

2.2. *Numerical simulation algorithm*

The simulations are made with a pseudospectral code (Haidvogel 1985; McWilliams 1984) which solves

$$\partial_t \kappa + J(\psi, \kappa) = [\nu_2 \Delta - \nu_4 \Delta^2]\omega, \tag{7}$$

where

$$\left.\begin{aligned} \kappa &= -\Delta\psi + \gamma^2\psi, \\ \omega &= -\Delta\psi. \end{aligned}\right\} \tag{8}$$

in the periodic domain $[-\pi, \pi] \times [-\pi, \pi]$, where $J(\psi, \kappa) = \partial_x \psi \, \partial_y \kappa - \partial_y \psi \, \partial_x \kappa$ and γ^{-1} is a constant called the Rossby deformation radius. Conventionally, κ is called the potential vorticity and ω is called the relative vorticity. The stream function ψ is normalized such that its area integral over the box vanishes. This has no physical importance since the velocity field is unaffected. For numerical reasons a uniform background is added to the vorticity field such that the box has zero circulation. This background vorticity has no influence on the evolution of the physical quantities as discussed in the Appendix. All runs in §§3 and 4 are with $\gamma = 0$.

In (6), $\nu_2 \Delta\omega$ is the Navier–Stokes viscosity term and $\nu_4 \Delta^2\omega$ is a hyperviscosity term. In this paper we discuss mainly $\nu_2 = 0$ and ν_4 finite, for this allows a higher effective Reynolds number, $Re_4 \equiv \Gamma^2/\nu_4 \omega_p$, on a given mesh as will be discussed in a future paper. Our simulations include $128^2/2$ and $256^2/2$ independent modes corresponding to 128^2 and 256^2 lattice intervals, respectively.

2.3. *Diagnostics*

To quantify the nonlinear evolutions, we use a set of diagnostic algorithms developed by Overman (Overman & Zabusky 1984). In essence this package constructs contours of a function defined on a finite mesh by specifying an *a priori* level. The contour, which in our case is always closed, is represented by two periodic cubic splines $[x(s), y(s)]$ where s is the arclength. This allows us to calculate moments of the domain bounded by the contour. In particular we calculate the second-order moments, which allows us to define an aspect ratio and orientation of an approximating ellipse, that we call the *diagnostic ellipse* of the contour. Furthermore, the package calculates the velocity components normal and tangential to the contour, as well as the maximum gradient of any function along the contour.

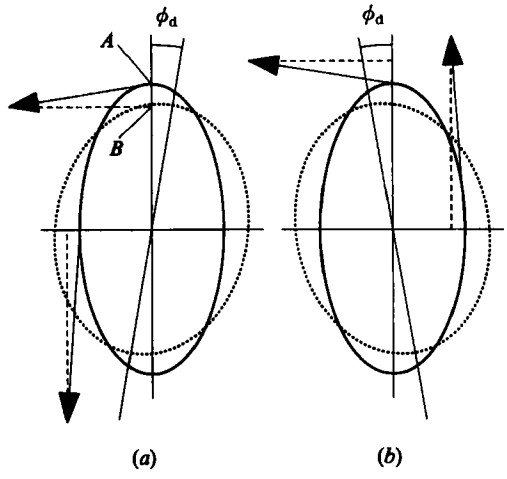

FIGURE 2. Sketch showing ——, a vorticity contour and · · · · ·, a nearby streamline. (*a*) $\phi_d > 0$, (*b*) $\phi_d < 0$. The arrows indicate the velocity field as obtained from the nearby streamline.

3. The axisymmetrization principle for inviscid vortex dynamics

In this section we quantify the axisymmetrization process by calculating the aspect ratio λ_ω of the diagnostic ellipses at different vorticity levels. We provide substantial computational evidence for the inviscid nature of the process. Finally, we derive a simple kinematic principle which the process obeys.

The basis for the discussion is the evolution of an initial $V(1, 20, 1.6, 0.8)$ vorticity distribution as shown in figure 8. In this figure the frames for $t \leqslant 3.0$ show the result of a 256^2-mesh calculation with $\nu_2 = \gamma = 0$ and $\nu_4 = 0.3125 \times 10^{-7}$. For $t > 3.0$ the pictures are obtained from a similar 128^2-mesh calculation with $\nu_4 = 5.0 \times 10^{-7}$.

3.1. *The inviscid nature of axisymmetrization*

In figure 3(*a–c*) the evolution of λ_ω at three different vorticity levels $\overline{\omega} = 5.0, 10.0, 15.0$ is shown. Also displayed is the aspect ratio λ_ψ of a streamline inside the vortex, $\overline{\psi} = -3.0$. We clearly observe a rapid initial decay in all aspect ratios. After the initial decay, λ_ω oscillates with a frequency and amplitude that is strongly dependent on the vorticity level $\overline{\omega}$. The aspect ratio of the streamline does not show similar fluctuations.

The fastest timescale for the relaxation towards axisymmetry is somewhat smaller than unity. For example, $\tau_\omega \equiv -\lambda_\omega/\dot{\lambda}_\omega \approx 0.8$ for $\overline{\omega} = 5.0$ at $t = 0.75$. The timescale related to dissipation is much larger. During the simulation the energy decay rate $\tau_E \equiv E/\dot{E}$ remains almost constant $\tau_E \approx 1.7 \times 10^5$. Thus the energy is nearly constant. A more sensitive dissipation timescale is obtained from the decay of the enstrophy $Z = \int \omega^2 \, dx \, dy$. Initially $\tau_Z \equiv -Z/\dot{Z} = 7.0 \times 10^5$ and decreases to a minimum of $\tau_Z = 161$ at $t = 1.775$. Afterwards it increases slowly to $\tau_Z = 304$ at the end of the simulation. Note, the pseudospectral algorithm conserves the global vorticity centroid and the total circulation exactly. Furthermore $M = \int \omega(x^2 + y^2) \, dx \, dy$ is conserved when $\gamma = \nu_2 = 0$ and $\nu_4 \neq 0$, just as with the Euler equations.

In order to further substantiate our claim that the axisymmetrization process is inviscid, we have investigated the evolution of $V(1, 20, 1.6, 0.8)$ under the influence of different dissipations. Figure 4 compares the evolution of λ_ω at $\overline{\omega} = 10.0$ during

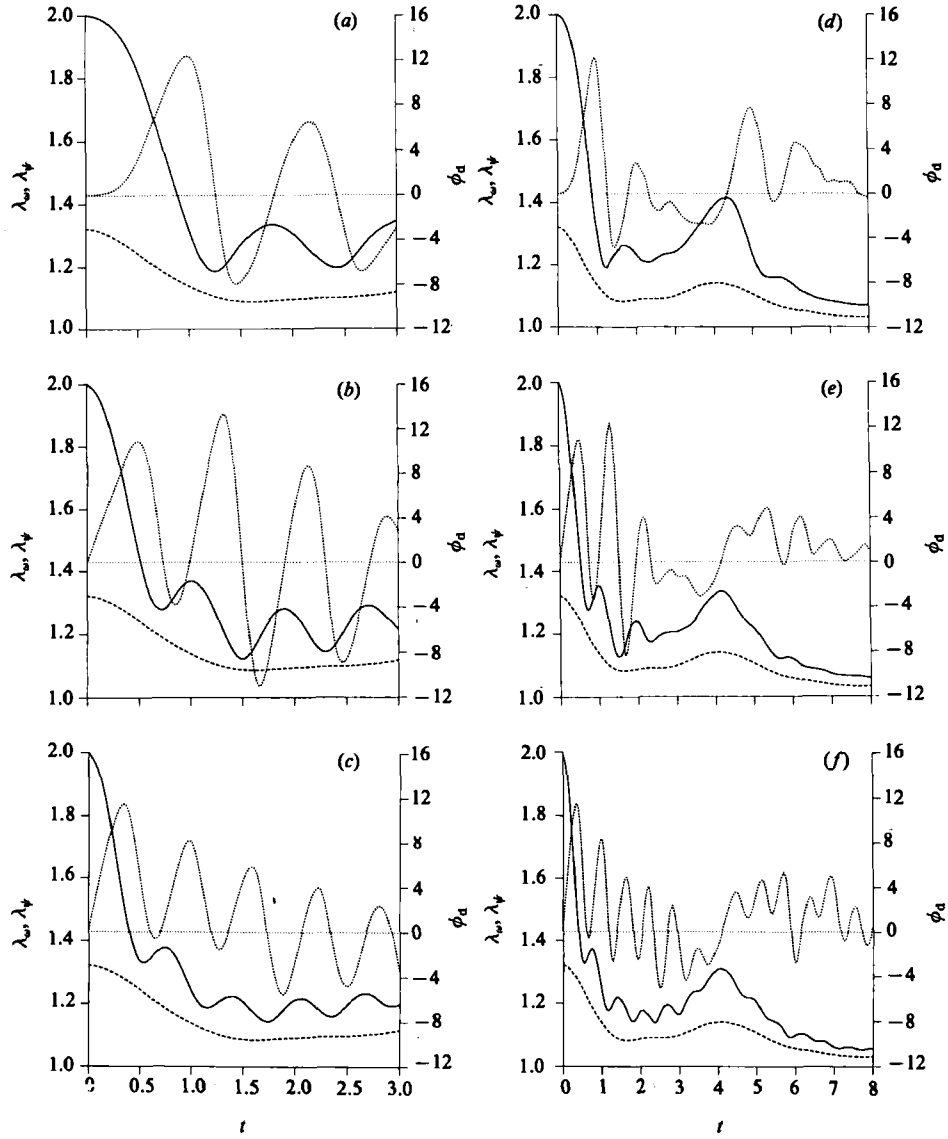

FIGURE 3. Evolution of ——, $\lambda_\omega(\overline{\omega}, t)$; – – – –, $\lambda_{\overline{\psi}}(t)$; · · · · ·, $\phi_d(\overline{\omega}, t)$ for the initial state $V(1, 20, 1.6, 0.8)$, corresponding to the physical plane results shown in figure 8. ϕ_d is measured in degrees. (*a*)–(*c*) show the diagnostics for a calculation on a 256^2 mesh with $\nu_2 = 0$ and $\nu_4 = 0.3125 \times 10^{-7}$. Note, $\lambda_{\overline{\psi}}$ is obtained from $\overline{\psi} = -3$, close to the extremity of the vortex (min $\overline{\psi} = -4.9$). (*a*) $\overline{\omega} = 5$, (*b*) $\overline{\omega} = 10$, (*c*) $\overline{\omega} = 15$. (*d*)–(*f*) show the diagnostics for the same calculation on a 128^2 mesh with $\nu_2 = 0$ and $\nu_4 = 5.0 \times 10^{-7}$. (*d*) $\overline{\omega} = 5$, (*e*) $\overline{\omega} = 10$, (*f*) $\overline{\omega} = 15$.

three different simulations. The solid curve is obtained from figure 3(*b*), whereas the dashed curve represents the 128^2-mesh calculation with $\nu_4 = 5.0 \times 10^{-7}$, a 16 times increase in ν_4. If the dissipation was the essential mechanism then τ_ω would be 16 times smaller. This is clearly not the case – the main relaxation towards axisymmetry occurs on the same timescale. Particularly we observe exactly the same initial decay of λ_ω. The dotted curve originates from a 128^2-mesh calculation with $\nu_4 = 0$ and $\nu_2 = 3.8 \times 10^{-4}$. Again we observe the same overall decay in λ_ω. Finally we remark

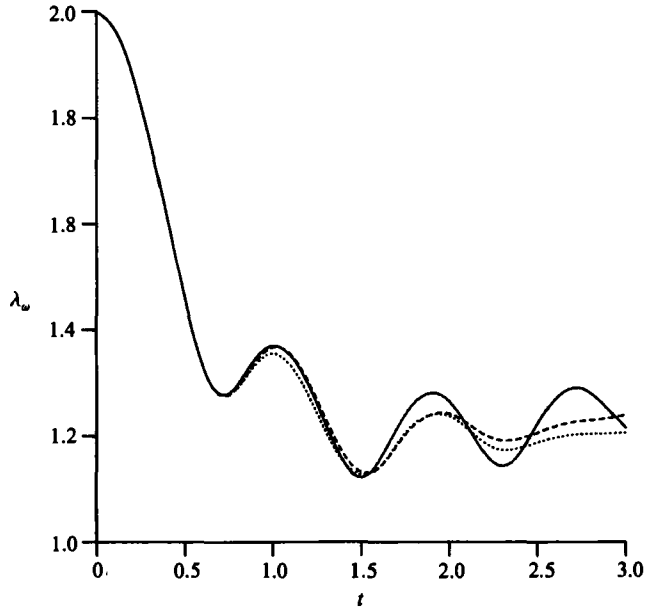

FIGURE 4. The evolution $\lambda_\omega(10, t)$ for $V(1, 20, 1.6, 0.8)$ is shown under the influence of different dissipations. ——, $\nu_4 = 0.3125 \times 10^{-7}$, $\nu_2 = 0$; – – – –, $\nu_4 = 5.0 \times 10^{-6}$, $\nu_2 = 0$; · · · · ·, $\nu_4 = 0$, $\nu_2 = 3.8 \times 10^{-4}$.

that the periodic boundary conditions applied in the pseudospectral code have no significant influence on the process. On the basis of the above discussion, we conclude that the axisymmetrization is an inviscid mechanism.

3.2. *Heuristic derivation of the axisymmetrization principle*

We now show that the axisymmetrization, of an isolated nearly elliptical vortex in an inviscid fluid can be related to the relative orientation of equivorticity lines and streamlines. As seen in figure 8 the low-amplitude vorticity contours develop a complicated structure including long spiral filaments. However, the contours at higher amplitudes remain nearly elliptical. Let us consider one of these contours, $\omega = \overline{\omega}$.

Using second-order moments of the domain enclosed by the vorticity contour $\omega = \overline{\omega}$, we obtain an aspect ratio $\lambda_\omega(\overline{\omega}, t)$ and an orientation $\phi_\omega(\overline{\omega}, t)$. Similarly we define $\lambda_\psi(\overline{\psi}, t)$ and $\phi_\psi(\overline{\psi}, t)$ for a closed streamline. From numerical simulations like figure 8 we have found that for streamlines in the vicinity of an assigned vorticity contour $\lambda_\psi(\overline{\psi}, t)$ and $\phi_\psi(\overline{\psi}, t)$ are almost independent of $\overline{\psi}$. For simplicity in the following heuristic derivation, we shall assume $\lambda_\psi(\overline{\psi}, t) = \lambda_\psi(t)$ and $\phi_\psi(\overline{\psi}, t) = \phi_\psi(t)$, independent of $\overline{\psi}$.

The streamfunction ψ is given in terms of ω by

$$\psi(x, y) = -\tfrac{1}{4}\pi \int\int \omega(\xi, \eta) \ln\left((x-\xi)^2 + (y-\eta)^2\right) \mathrm{d}\xi \, \mathrm{d}\eta, \tag{9}$$

which is the inversion of (8), ($\gamma = 0$). That is ψ is obtained as a weighted integral over the vorticity field ω. If $\omega(x, y)$ has the mirror symmetries of an ellipse, it follows from (9) that ψ has the same symmetries. This applies to the initial conditions in figure 8. As time increases, the mirror symmetries of the vorticity field are broken

by the formation of filaments. Thus at later times we consider the vorticity field as the superposition of a symmetric component ω_s, with the symmetries of an ellipse, and an asymmetric component ω_a:

$$\omega(x,y) = \omega_s(x,y) + \omega_a(x,y). \tag{10}$$

It follows from the linearity of the integral in (9) that ψ can also be viewed as the sum of symmetric and asymmetric components

$$\psi(x,y) = \psi_s(x,y) + \psi_a(x,y). \tag{11}$$

Clearly at $t = 0$ in figure 8 we have $\omega = \omega_s$ and $\psi = \psi_s$. We observed from the evolution pictures, that at high-vorticity amplitudes the asymmetric term, ω_a, in (10) is negligible; hence it is reasonable to assume that $\phi_\omega(\overline{\omega}, t) \approx \phi_{\omega_s}(\overline{\omega}, t)$ at such amplitudes. Although ω_a has little influence on ϕ_ω at high-vorticity amplitudes, ω_a has a significant influence on ψ_a as is evidenced through (9); this in turn produces an effect on ϕ_ψ through (11).

In figure 8 at $t = 0.5$ the filaments which are forming at the lower-vorticity contours are accounted for by ω_a, hence these filaments cause $\phi_\omega(\overline{\omega}, t)$ to depart from $\phi_\psi(t)$. In fact $\phi_\omega(\overline{\omega}, 0.5) > \phi_\psi(0.5)$ at high-vorticity contours. This consideration justifies the introduction of the difference angle ϕ_d:

$$\phi_d(\overline{\omega}, t) \equiv \phi_\omega(\overline{\omega}, t) - \phi_\psi(t). \tag{12}$$

In figure 2 we investigate the consequences of ϕ_d positive and ϕ_d negative. The solid curve represents a high-amplitude vorticity contour and the dotted curve is a nearby streamline. Since we have already shown that axisymmetrization is an inviscid process, we may assume $D_t \omega = 0$ (the vorticity of each fluid particle is conserved); the velocity field along the vorticity contour thereby yields the short-time deformation of the contour. The velocity fields along $\omega = \overline{\omega}$ can be constructed from the streamlines. This construction becomes particularly simple with the assumptions $\lambda_\psi(\overline{\psi}, t) = \lambda_\psi(t)$ and $\phi_\psi(\overline{\psi}, t) = \phi_\psi$. For example in figure 2(*a*), since the streamline through A (not shown) has the same slope as the streamline through point B, the direction of the velocity vector at point A is obtained as the tangent to the streamline at point B. With further evolution the major axis of the elliptical vorticity contour will decrease due to the fact that the projection of the velocity vector at A on the major axis is negative. Similarly, the minor axis will increase. Hence the aspect ratio λ_ω will decrease, that is $d_t \lambda_\omega$ is negative when ϕ_d is positive. A similar argument using figure 2(*b*) shows $d_t \lambda_\omega > 0$ when $\phi_d < 0$. From the above, we derive the inequality

$$d_t \lambda_\omega(\overline{\omega}, t)\, \phi_d(\overline{\omega}, t) \leqslant 0. \tag{13}$$

This is the *axisymmetrization principle* for a nearly elliptical vorticity distribution and as described in the next section it is essential for understanding the axisymmetrization process.

We validate (13) by examining the diagnostics λ_ω, $\phi_d(\overline{\omega}, t)$ and $\lambda_\psi(t)$ contained in the panels of figure 3. These are obtained for $\overline{\omega} = 5, 10, 15$ from two simulations showing the evolution of $V(1, 20, 1.6, 0.8)$. The axisymmetrization principle (13) predicts the extrema of $\lambda_\omega(\overline{\omega}, *)$ coincide in time with the zeros of $\phi_d(\overline{\omega}, *)$. Figure 3 shows this prediction is true within a very good approximation. A small discrepancy is seen at $t = 0.5$ for $\overline{\omega} = 15.0$, this discrepancy might be due to the coarse time-sampling of output results taken at $\Delta t = 0.125$.

We shall now derive an approximation for $d_t \lambda_\omega(\overline{\omega}, t)$ at high-vorticity contours. In

the neighbourhood of the vorticity contour $\omega = \overline{\omega}$ we approximate the stream function by a quadratic polynomial

$$\psi(x,y) \approx \Psi(x,y) = c_1 x^2 + c_2 xy + c_3 y^2, \tag{14}$$

where the constants c_1, c_2 and c_3 are related to ϕ_ψ and λ_ψ in the following way:

$$c_1 = c[\cos^2\phi_\psi + \lambda_\psi^2 \sin^2\phi_\psi],$$
$$c_2 = c[(1-\lambda_\psi^2)\sin 2\phi_\psi].$$
$$c_3 = c[\sin^2\phi_\psi + \lambda_\psi^2 \cos^2\phi_\psi],$$

Here c is a constant determined from $\overline{\omega}$

$$\overline{\omega} = -\Delta\Psi = -2c(1+\lambda_\psi^2),$$

or

$$c = -\tfrac{1}{2}\overline{\omega}(1+\lambda_\psi^2)^{-1}.$$

In order to calculate the evolution of λ_ω we define moments of the region D enclosed by the vorticity contour $\omega = \overline{\omega}$,

$$J^{mn} \equiv \int_D x^m y^n \,\mathrm{d}\sigma. \tag{15}$$

Using the approximation (14) we find

$$d_t J^{mn} = \int_D [m x^{m-1} y^n \Psi_y - n x^m y^{n-1} \Psi_x]\,\mathrm{d}\sigma,$$
$$= -2c_1 n J^{m+1,\,n-1} + c_2(m-n) J^{mn} + 2mc_3 J^{m-1,\,n+1}. \tag{16}$$

For an ellipse with aspect ratio λ, orientation ϕ and area A we have

$$J^{20} = \frac{A^2(\lambda^2 + (1-\lambda^2)\sin^2\phi)}{4\pi\lambda}, \tag{17}$$

$$J^{02} = \frac{A^2(\lambda^2 + (1-\lambda^2)\cos^2\phi)}{4\pi\lambda}, \tag{18}$$

$$J^{11} = -\frac{A^2(1-\lambda^2)(\sin 2\phi)}{8\pi\lambda}, \tag{19}$$

which implies

$$d_t(J^{20} + J^{02}) = \frac{A^2}{4\pi} d_t(\lambda_\omega + \lambda_\omega^{-1}). \tag{20}$$

On the other hand (16) yields

$$d_t(J^{20} + J^{02}) = 2c_2(J^{20} - J^{02}) + 4(c_3 - c_1) J^{11}. \tag{21}$$

We substitute (17)–(19) into (21), equate the right-hand sides of (20) and (21) and obtain

$$d_t \lambda_\omega = 2c(1-\lambda_\psi^2)\lambda_\omega \sin 2(\phi_\omega - \phi_\psi),$$
$$= \frac{-\overline{\omega}(1-\lambda_\psi^2)\lambda_\omega}{(1+\lambda_\psi^2)} \sin 2\phi_d. \tag{22}$$

We have compared this approximation with $d_t\lambda_\omega$ obtained by differentiating the cubic-spline interpolation of λ_ω shown in figure 3 (*a*, *b*). The comparison is shown in figure 5 for $\overline{\omega} = 15.0$ and 10.0. The dotted curve represents the approximation (22). Note that for $\overline{\omega} = 5$ the extrema disagree in amplitude by a factor three.

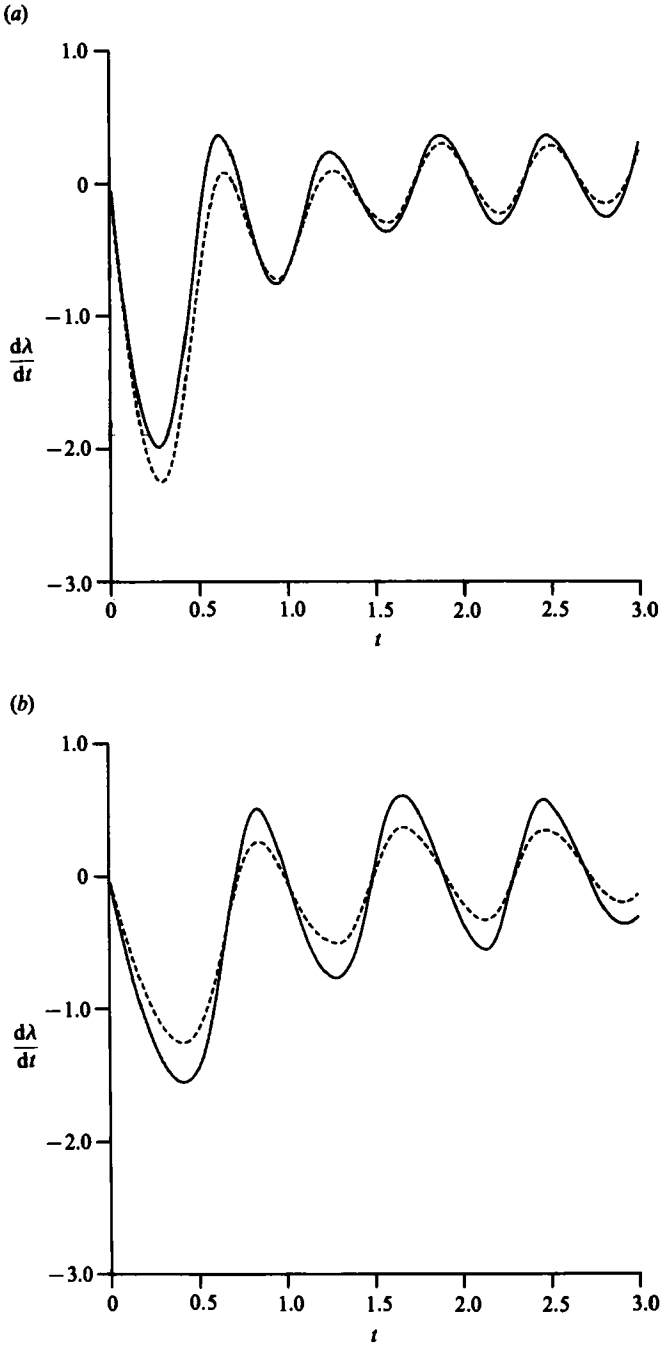

FIGURE 5. Comparison of ----, the approximation to $d_t \lambda_\omega(\bar{\omega}, t)$ given in (22) with ——, the true value as obtained by spline differentiation of λ in figure 3; (*a*) $\bar{\omega} = 15$, (*b*) $\bar{\omega} = 10$.

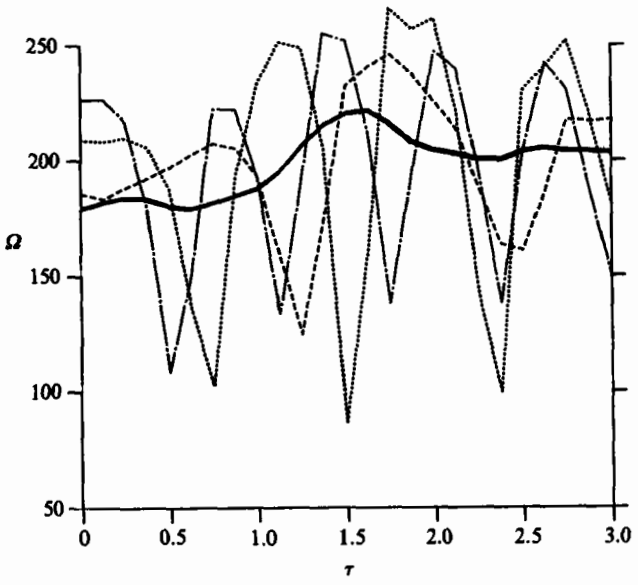

FIGURE 6. Variation of the angular velocity Ω (degrees/time unit) of the contours ----, $\overline{\omega} = 5$; · · · · ·, $\overline{\omega} = 10$; -·-·-, $\overline{\omega} = 15$ and ——, $\overline{\psi} = -3$ for the evolution of $V(1, 20, 1.6, 0.8)$, (corresponding to figure 3*a–c*).

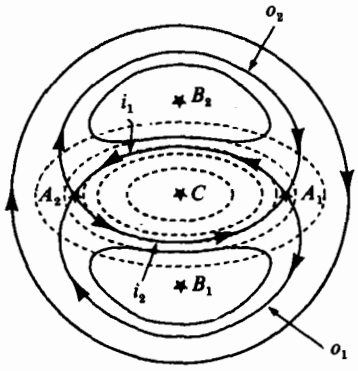

FIGURE 7. Composite sketch of ——, the corotating stream function ψ_c and ----, the vorticity field. Indicated are two saddle points A_1 and A_2, three centres B_1, B_2, C and the separatrix lines connecting the saddle points.

4. Kinematic description of the relaxation process

In this section we apply the axisymmetrization principle to explain the evolution of the $V(1, 20, 1.6, 0.8)$ vortex. The aspect ratio clearly is in the stable regime of the Kirchhoff vortices. However, the dynamics are very different.

A critical understanding of the vortex's deformation is obtained by examining contours of a corotating stream function

$$\psi_c = \psi + \tfrac{1}{2}\Omega(t)\,(x^2 + y^2), \tag{23}$$

where $\Omega(t)$ is an appropriate angular velocity discussed below. The choice of Ω is important, for streamfunctions observed in different reference frames yield different

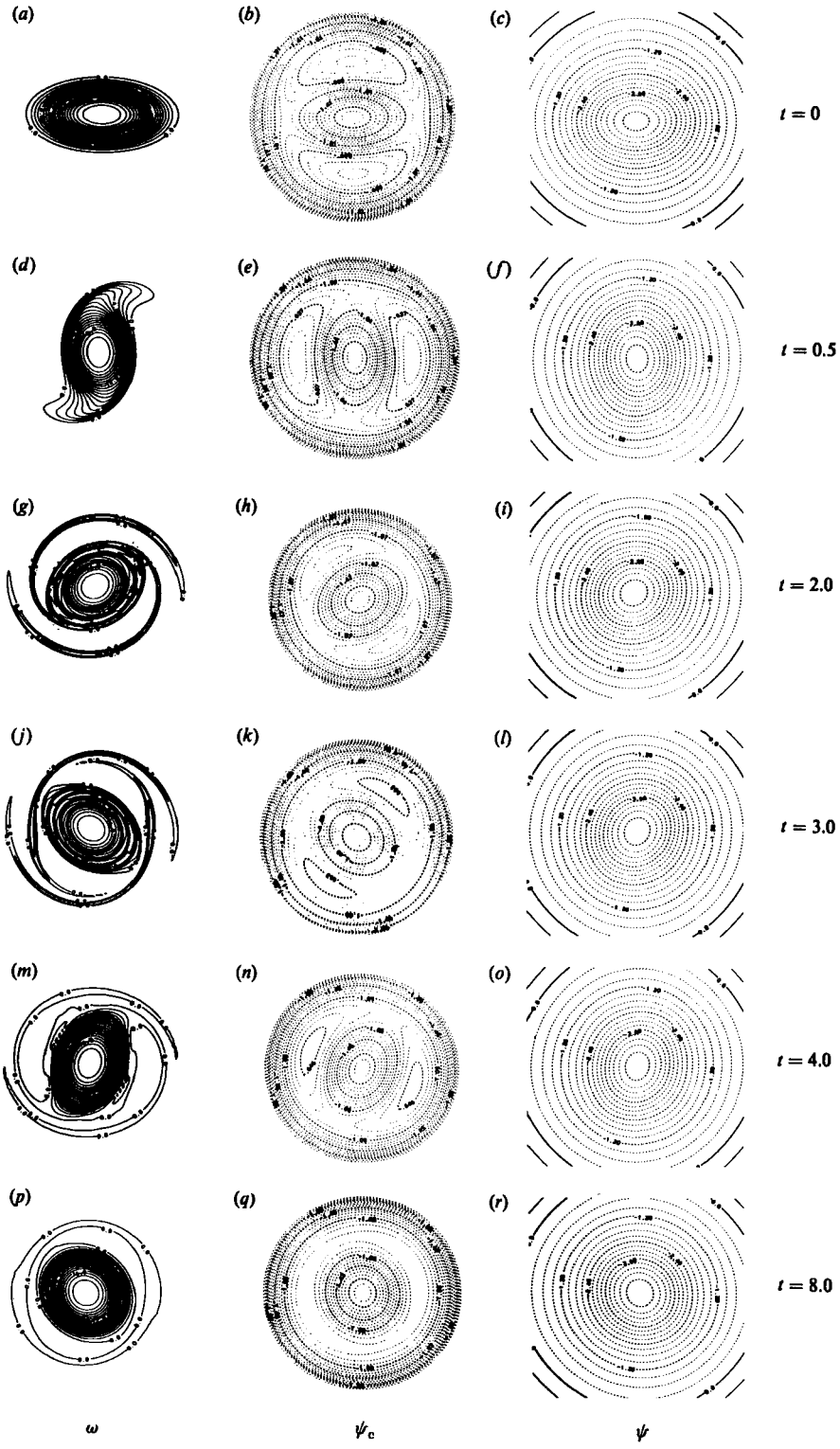

FIGURE 8. The evolution of $V(1, 20, 1.6, 0.8)$ at $t = 0$, 0.5, 2, 3, 4 and 8. Column 1 shows ω; column 2 ψ_c; column 3 ψ; For $t \leqslant 3$ the pictures show the result of a 256^2-mesh calculation with $\nu_4 = 0.3125 \times 10^{-7}$. For $t \geqslant 3$ the mesh is 128^2 and $\nu_4 = 5.0 \times 10^{-7}$.

views, as described by Perry, Chong & Lim (1982). We may consider two possibilities: the angular velocity of a mid-level $\overline{\omega}$-ellipse, or a mid-level $\overline{\psi}$-ellipse (the lower-lying vorticity contours tend to break and are therefore not useful). The latter is preferred since it results from a weighted average of the vorticity field, and therefore shows much smaller fluctuations during the evolution, as shown in figure 6. Note that the period of the oscillations of Ω in figure 6 is smaller for higher-vorticity contours and agree with those of λ_ω in figure 3. Hence, we define Ω as the instantaneous angular velocity

$$\Omega(t) = d_t \phi_\psi. \tag{24}$$

Figure 7 shows a composite sketch of ω and ψ_c for the $V(1, 20, 1.6, 0.8)$ at $t = 0$, where $\Omega = 3.14$. We see five stagnation points: A_1 and A_2 are saddle points, B_1 and B_2 are centres of clockwise circulation created by transforming to a rotating frame, while C is the original centre of counterclockwise circulation. The saddle points are connected by four separatrices: the inner ones, i_1 and i_2 and the outer ones, o_1 and o_2. The domains surrounding the centres B_1, C and B_2 which are bounded by the nearest separatrices, we designate $\mathscr{B}_1$, $\mathscr{C}$ and $\mathscr{B}_2$, where we call $\mathscr{B}_1$ and $\mathscr{B}_2$ 'ghost vortices'. These vanish as the aspect ratio of the vorticity core approaches unity. We have observed that the location of the separatrices and the stagnation points changes slowly compared to the bulk rotation, which is almost constant in time. Therefore the streamlines in the corotating frame are useful for describing the differential deformation of the vortex.

The angle ϕ_d can be non-zero only when the vorticity field as a whole is distorted from the mirror symmetry of an ellipse. Therefore we again describe the vorticity field as a superposition of a symmetric and an asymmetric field,

$$\omega = \omega_s + \omega_{a,f} + \omega_{a,c}. \tag{25}$$

The dominant asymmetric term, $\omega_{a,f}$, is caused by the filaments as seen by inspection of the vorticity field at $t = 0.5$, see figure 8(*d*). This accounts for the overall nature of the relaxation process, displayed in the aspect ratio of the streamlines $\lambda_\psi(t)$. Component $\omega_{a,c}$ results from the distortion from elliptical symmetry in the core of the vortex. This distortion is a secondary effect caused by differential rotation and gradient intensification and is responsible for the small-amplitude oscillations in $\lambda_\omega(\overline{\omega}, t)$, see figure 3(*a–c*).

4.1. *The influence of the filaments on the core*

We now present a qualitative discussion of the effects of asymmetries in the vortex field on the evolution of the vorticity. It is convenient to describe the effects over approximately four 'eddy-rotation' times in four phases.

At $t = 0$, see figure 8(*b*), the saddle points A_1 and A_2 are located along the major axis and we observe, crucially, that they lie inside the region of vorticity. Thus the vorticity outside the region $\mathscr{C}$ will convect away and form filaments. Only the lower quarter of the vorticity contours will be affected by the shedding, while the higher contours will remain almost elliptical since they are contained in $\mathscr{C}$. This prediction based on figure 7 agrees with the actual vorticity field at $t = 0.5$, see figure 8(*d*). At $t = 0.5$ the vortex is shedding filaments and a smaller core is forming. Comparison of the vorticity field with the ψ_c-field illustrates how the filaments are wrapping around the regions $\mathscr{B}_1$ and $\mathscr{B}_2$. Through the first time unit the filaments contribute strongly to the asymmetric component of the vorticity field. Hence the diagnostic ellipses of the ψ-streamlines lag slightly behind the higher-vorticity contours, a consequence of the smoothing implied in (9). Thus the angle $\phi_d > 0$. Figure 3 shows

that ϕ_d becomes as large as 12°. According to the axisymmetrization principle (13) the aspect ratio λ_ω must decrease rapidly. As seen in figure 3(*b*) $\lambda_\omega(10.0)$ drops from 2.0 to 1.3 within a quarter of revolution ($t = 0.5$). Meanwhile the aspect ratio of the ψ-streamlines decreases from 1.32 to 1.23.

During the second phase (from $t \approx 1.5$ to $t \approx 2.5$) λ_ψ is approximately constant, because the filaments hardly contribute to the asymmetry. Namely, they are situated almost symmetrically around the midpoints of the outer separatrices o_1 and o_2, see figure 8(*g*). The shedding of vorticity has stopped because the core is entirely contained in $\mathscr{C}$ and most of the low-amplitude vorticity is now in the filaments. Note that the vorticity gradient is larger along the outer side of the filaments than along the inner. The reason is that the vorticity outside the outer separatrices is convected faster into the filaments than the vorticity inside $\mathscr{B}_1$ and $\mathscr{B}_2$. Also note that the filaments maintain a positive curvature, that is they do not show any sign of 'roll-up' because of the strain induced by the core. Furthermore, the vorticity tends to zero slowly near the tip of the filaments causing the phenomenon of 'tip' roll-up to occur on a slower timescale than in contour dynamical simulations like figure 9 of Overman & Zabusky (1982) which shows an indication of tip roll-up. Note that the transport of vorticity in the filaments is essentially an inviscid process, since the circulation is conserved and the effect of dissipation is to spread the vorticity normal to the axes of the filaments.

The third phase of the evolution lasts from $t \approx 2.5$ to $t \approx 4.0$. The filaments are now out of their previous 'symmetric' position and do again contribute to a non-zero ϕ_d. However, the new position of the arms yields a negative ϕ_d and thus λ_ψ increases. During this phase the stretching of the filaments becomes complicated. As seen by comparing figures 8(*j* and *k*), part of the filaments are trapped inside $\mathscr{B}_1$ and $\mathscr{B}_2$, resulting in a concentration of vorticity near stagnation points A_1 and A_2. This vorticity reattaches to the core and reverses the propagation direction in the corotating frame as the particles are convected along i_1 and i_2.

The fourth phase begins at $t \approx 4.0$ when the non-reattached parts of the filaments are convected so far around the core that they contribute to a positive ϕ_d leading to another relaxation towards axisymmetry. A weak secondary breaking of the core follows because the saddlepoints A_1 and A_2 have moved slightly into the core, compare figures 8(*m* and *n*). Note that figures 8(*m–r*) are the result of a 128^2 mesh calculation and therefore the gradients are less steep than in the previous figures. Figure 8(*p*) shows the vortex at $t = 8.0$, where $\lambda_\psi = 1.05$ and $\lambda_\omega(10) = 1.1$.

For any weakly dissipative fluid we believe the state in figure 8(*p*) is close to the final one, which is a nearly circular core surrounded by a nearly concentric ring. Figure 9 shows cross-sections of the vortex along the major and minor axes. The core has a steeper gradient along the lower-vorticity contours than along the higher ones. This follows from the fact that most of the fluid particles carrying small-amplitude vorticity at $t = 8.0$ have been convected away from the core and into the ring. Note that in recent calculations with a contour dynamical algorithm ($\nu_2 = \nu_4 = 0$) and comparable initial conditions, D. G. Dritschel (1986, private communication) observed similar phenomena and the near-concentric ring was composed of small-scale low-amplitude filaments in a spiral pattern.

4.2. *The effects of asymmetry in the vortex core*

As seen in figure 8(*g*) the vortex core is slightly distorted from elliptical symmetry by the presence of inward-spiralling steep-gradient regions. These are caused by a

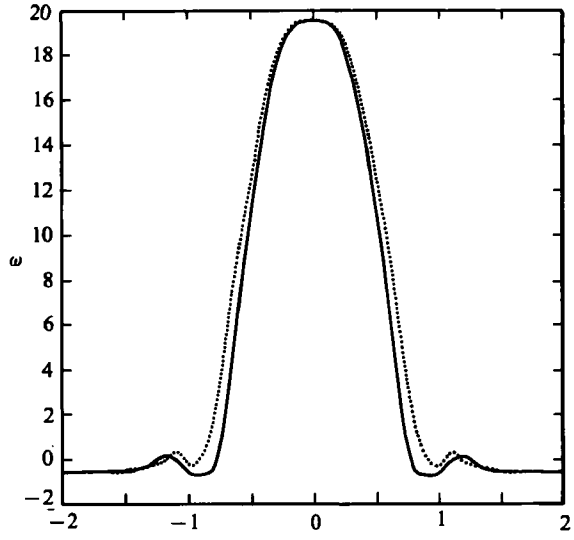

FIGURE 9. Cross-sections along ····, the major and ——, minor axes of the vorticity field at $t = 8$ in figure 8.

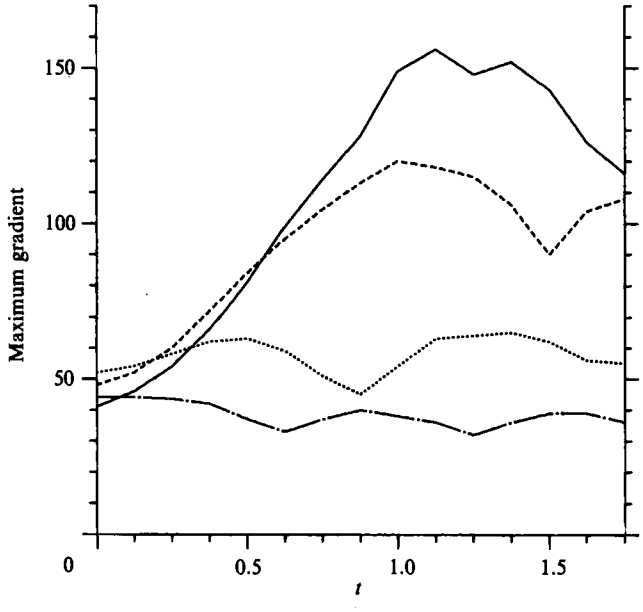

FIGURE 10. The maximum gradient along a vorticity contour $\mathrm{Max}\,|\nabla\omega(s)|$, for the evolution of $V(1, 20, 1.6, 0.8)$ on a 256^2 mesh (corresponding to figure 3*a–c*). ——, $\overline{\omega} = 3$; – – – –, $\overline{\omega} = 5$; · · · · ·, $\overline{\omega} = 10$; –·–·–, $\overline{\omega} = 15$.

differential rotation in region $\mathscr{C}$ of the core which is due to the variation of the stream-function profiles. This effect is responsible for the fine-scale oscillations of λ_ω whose frequency increases with ω as seen in figure 3. The quantitative aspects of this correlation are not fully understood. (Note, the filaments cannot cause the frequency to be strongly dependent on the contour level as evidenced by (9)).

Just as with filament formation, convection of vorticity along separatrix lines is the main cause of the observed vorticity gradient intensification and it occurs at the

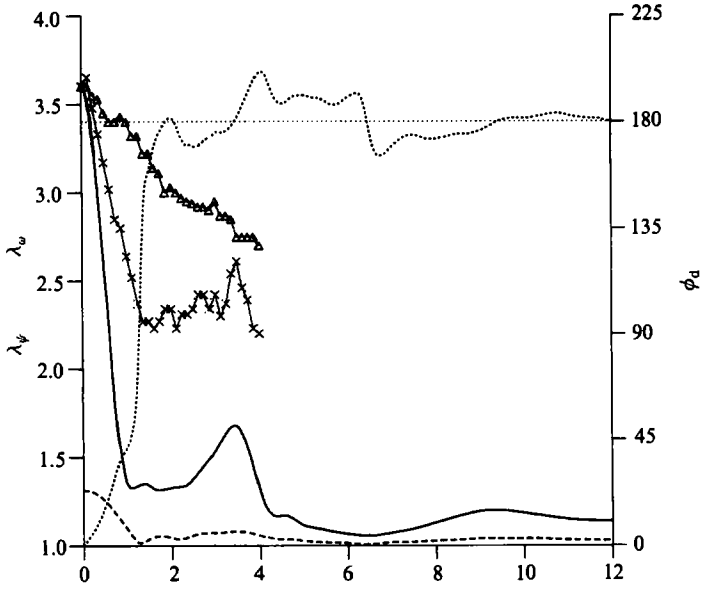

FIGURE 11. Evolution of ——, $\lambda_\omega(10,t)$, – – – –, $\lambda_{\dot{\psi}}(t)$ and · · · · ·, $\phi_d(10,t)$ for the initial state $V(1,20,1.44,0.4)$ on a 128^2 mesh with $\nu_4 = 5.0\times10^{-7}$, corresponding to the physical plane results shown in figure 12. (Note $\lambda_{\dot{\psi}}$ is obtained from $\overline{\dot{\psi}} = -1.2$, close to the extremity of the vortex). Also shown are evolutions of $\lambda_\omega(10,t)$ —×—, $V(0.5,20,1.44,0.4)$ and —△—, $V(0.2,20,1.44,0.4)$ on a 256^2 mesh with $\nu_2 = 0$ and $\nu_4 = 0.3125\times10^{-7}$, corresponding to columns 2 and 3 in figure 12.

lower contours. Until $t \approx 0.5$ the gradient intensified regions contribute to ϕ_d in the same way as the filaments. However, at later times the high-gradient regions are mostly contained in $\mathscr{C}$ and therefore convection (differential rotation) in the core gives rise to a spiral gradient band, e.g. see figure 8(*g*). For reasons we do not understand, the spiral approaches the centre of the core and thereby affects higher and higher vorticity levels as time progresses. At $t = 0$ the ψ-profile is almost linear in an elliptical annulus around the centroid of the vortex. This implies a differential rotation, which contributes initially to the gradient steepening, but later on becomes very complicated. For example, higher contours sometimes rotate faster and sometimes slower than the lower contours, a phenomenon associated with the λ_ω oscillations.

It is not known if there is an inviscid limit to the gradient steepening. Our simulations indicate only a numerical limit associated with finite resolution. Figure 10 shows the maximum gradient along four contours ($\overline{\omega} = 3$, 5, 10 and 15) for the 256^2 calculation. Initially, for $\overline{\omega} = 3$ and 5, the calculated maximum gradients vary smoothly with the arclength, but for $t > 0.6$ one observes small-scale modulations due to the finite resolution. The saturation of the maximum gradient at $t \approx 1.0$ for $\overline{\omega} = 3$, we believe is due to inadequate grid resolution. The oscillations on $\overline{\omega} = 10$ and $\overline{\omega} = 15$ are correlated with the λ_ω variations. Calculations on 64^2 and 128^2 meshes yield the same phenomenon, except that the maximum gradient saturates earlier.

5. Dependence on initial conditions and other parameters

Our main example discussed above has an aspect ratio in the stable Kirchhoff regime. For $\delta = 1$ distributions with aspect ratios in the unstable Kirchhoff regime ($\lambda > 3$), a faster decrease of the aspect ratio is observed because more vorticity is

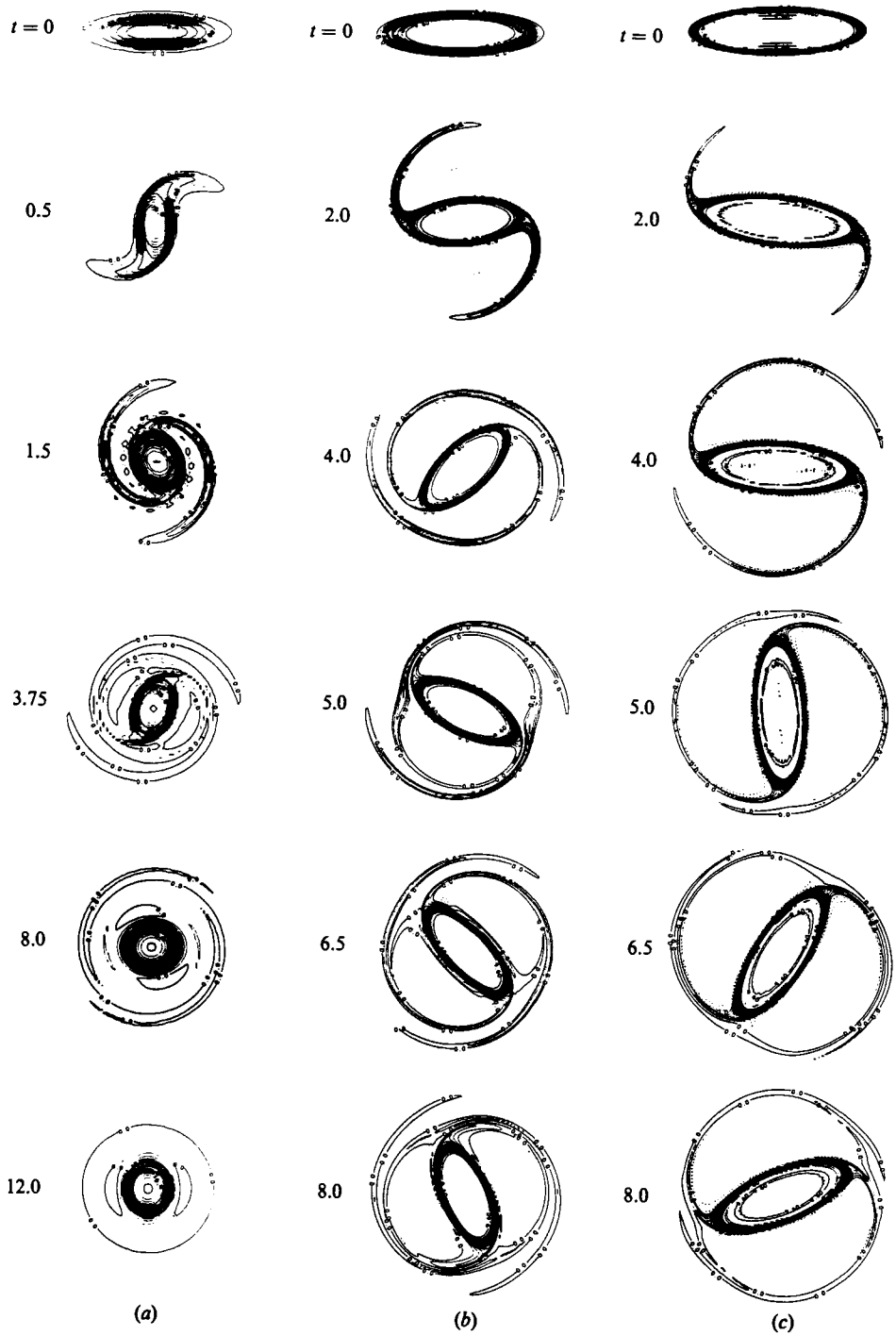

FIGURE 12. (*a*) Evolution of ω for $V(1, 20, 1.44, 0.4)$ on a 128^2 mesh with $\nu_2 = 0$ and $\nu_4 = 5 \times 10^{-7}$. (*b*) Evolution of ω for $V(0.5, 10, 1.44, 0.4)$ on a 256^2 mesh with $\nu_2 = 0$ and $\nu_4 = 0.3125 \times 10^{-7}$. (*c*) Evolution of ω for $V(0.2, 10, 1.44, 0.4)$ on 256^2 mesh with $\nu_4 = 0.3125 \times 10^{-7}$. The times are the same as in (*b*). The small overshoot contours in the core and ----, negative contours near the filaments are the result of $\nu_4 \Delta^2$ dissipation.

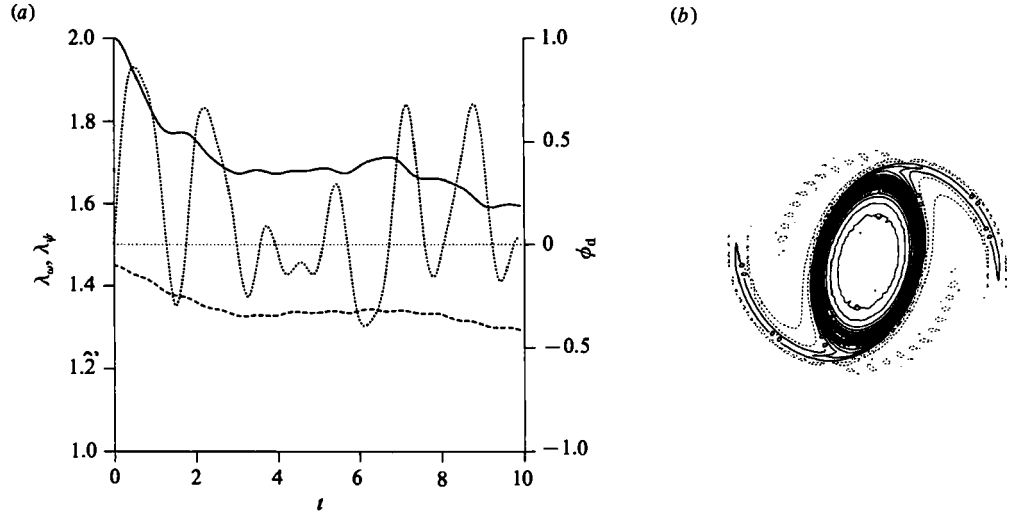

FIGURE 13. (a) Evolution of ——, $\lambda_\omega(7.2, t)$, – – – –, $\lambda_\psi(t)$ and · · · · ·, $\phi_d(7.2, t)$ for the initial state $V(0.5, 9.54, 1.6, 0.8)$ on a 128^2 mesh with $\nu_2 = 0$ and $\nu_4 = 5.0 \times 10^{-7}$. (Note ϕ_d is measured in degrees. Note λ_ψ is obtained from $\overline{\psi} = -3.6$, close to the extremity of the vortex.) (b) The vorticity field ω at $t = 2.5$ showing the filaments.

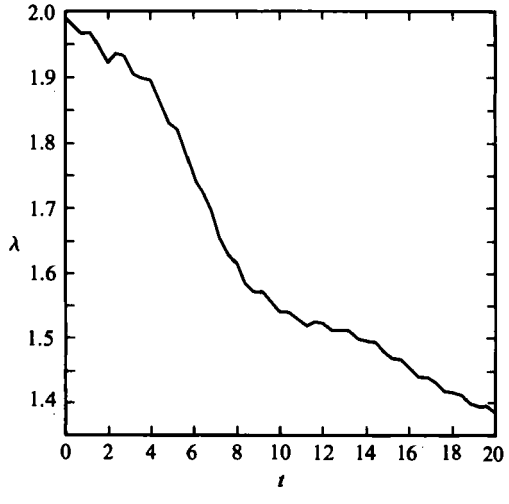

FIGURE 14. Evolution of $\lambda_\omega(3.2, t)$ for the initial state $V(0.2, 6.68, 1.6, 0.8)$ on a 64^2 mesh with $\nu_4 = 8.0 \times 10^{-6}$.

shed into the filaments causing a greater value of ϕ_d. For example, for $V(1, 20, 1.44, 0.4)$, ϕ_d becomes as large as 180°, as shown in figure 11. It is interesting to observe that the first phase of the bulk relaxation still lasts approximately one half revolution, and that during this period $\lambda_\omega(10)$ relaxes to 1.3, which is approximately the same value as in the main case. In figure 12(a) we see that the filaments contain more vorticity than previously and the third phase of the relaxation is more evident. Note the secondary breaking ($t = 3.75$) and the complicated structure of the filaments.

As we decrease δ the initial vorticity distribution approaches the Kirchhoff

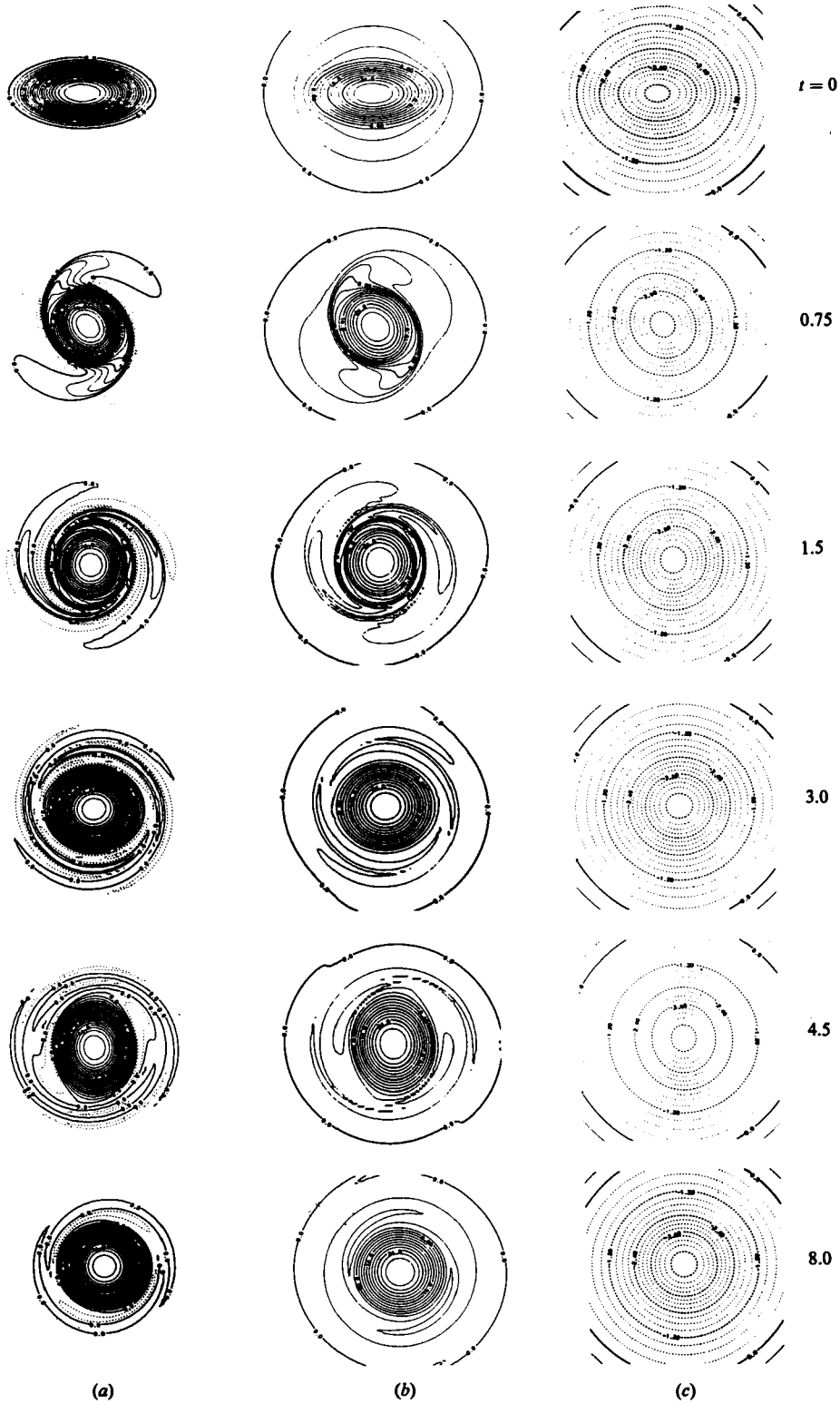

FIGURE 15. The evolution of (*a*) ω, (*b*) κ and (*c*) ψ for an initial $V(1, 20, 1.6, 0.8)$ distribution of ω with $\gamma = \sqrt{2}$ on a 128^2 mesh with $\nu_4 = 5.0 \times 10^{-7}$.

elliptical vortex, for which the saddle points A_1, A_2 and the inner separatrices i_1, i_2 are outside the vorticity region. Hence the amount of vorticity initially shed into the filaments decreases with δ. Figure 12(*b* and *c*) shows the evolution of initial $V(0.5, 10, 1.44, 0.4)$ and $V(0.2, 10, 1.44, 0.4)$ distributions. Figure 11 shows how the contour dynamical limit is obtained as δ tends to zero. However, the convergence is not uniform in time, because we are approaching an unstable Kirchhoff elliptical vortex. The evolution of these near tophat distributions highlights the reattachment of the filaments. The second column of figure 12 shows how parts of the filaments get trapped in the ghost vortices $\mathscr{B}_1$ and $\mathscr{B}_2$. At $t = 5.0$ particles carrying low-amplitude vorticity accumulate near the stagnation points A_1 and A_2. These particles are convected along the core near inner separatrices at $t = 6.5$. Later ($t = 8.0$) these particles are again shed into filaments along the outer separatrices. The slight vorticity overshoot ($\omega > \omega_p$) within the core and negative vorticity regions near the filaments in figure 12(*c*) are the result of $\nu_4 \Delta^2$ dissipation. A detailed discussion of this minor effect will be given in the fourth paper in the series. The small-δ distribution, $V(0.5, 9.54, 1.6, 0.8)$, provides another comparison with contour dynamics, see figure 13. Again we observe the aspect ratio levels out after slightly more than half a revolution. Owing to the weak filaments, ϕ_d never exceeds 1° in magnitude and therefore the first relaxation phase causes λ_ω to decrease only to 1.6. However, this is a considerable difference from contour dynamics, and emphasizes the effect of weak filaments on the overall structure. Note, the correlation between small-δ and slow relaxation towards axisymmetry is due to the fact that Kirchhoff ellipse is a stable steady state for $\lambda < 3$.

In the case of a very small δ, dissipation plays an important role during the first few revolutions. Initially no vorticity is shed into filaments for sufficiently small values of δ. However, the dissipation relaxes the gradients, thereby generating a growing perturbation on the steady-state solution. As soon as the perturbation is large enough to generate filaments the axisymmetrization follows the usual pattern. Figure 14 illustrates the influence of the dissipation on the evolution of $V(0.2, 6.68, 1.6, 0.8)$ distribution. For $t < 4$ diffusive mechanisms are operating and for $t > 4$ the inviscid axisymmetrization mechanism takes over. The larger dissipation of this run also causes the fine-scale oscillations to be suppressed. This observation supports our conclusion that the fine-scale oscillations are caused by asymmetries in the vortex core and not by the filaments, because the fine structure in the core is smoothed by dissipation while the vorticity in the filaments remains near the outer separatrices.

5.1. *Geostrophic vortices*

Geostrophic vortices also relax inviscidly towards axisymmetry as shown in figure 15 ($\gamma = 2^{\frac{1}{2}}$). Again the driving mechanism is the departure of the vorticity field from elliptical symmetry – caused by filamentation. In comparison with figure 8 ($\gamma = 0$) we observe broader filaments and generation of negative vorticity, $\omega = -\Delta\psi$. Also the filaments are closer to the core. These differences become more pronounced with smaller deformation radius (larger γ).

In the absence of dissipation, the potential vorticity $\kappa \equiv \omega + \gamma^2\psi$ is convected with the flow, but the relative vorticity is not. The stream function is given in terms of the potential vorticity

$$\psi(x, y) = \frac{1}{2\pi} \int\int \kappa(\xi, \eta)\, K_0[\gamma((\xi - x)^2 + (\eta - y)^2)]^{\frac{1}{2}}\, \mathrm{d}\xi\, \mathrm{d}\eta, \tag{26}$$

where K_0 is the modified Bessel function of the second kind and zeroth order.

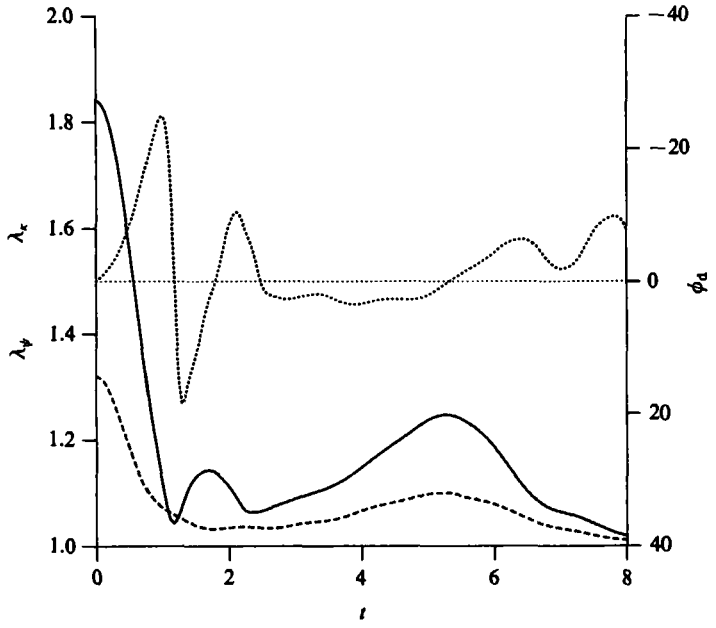

FIGURE 16. Evolution of ——, $\lambda_\kappa(10,t)$, – – – –, $\lambda_\psi(-3.2,t)$ and · · · · ·, ϕ_d for the potential vorticity of $V(1,20,1.6,0.8)$ with $\gamma = \sqrt{2}$ calculated on a 128^2 mesh with $\nu_2 = 0$ and $\nu_4 = 5\times10^{-7}$.

The axisymmetrization principle applies to contours of constant κ, the conserved quantity. Figure 16 shows diagnostics for the contour $\kappa = 10$ of the evolving vortex shown in figure 16. Cearly the axisymmetrization principle is valid. As compared with figure 3 ($\gamma = 0$) we observe the same qualitative behaviour of the aspect ratios λ_κ and λ_ψ. Note, there are no fine-scale oscillations in figure 16 and furthermore the higher contours of potential vorticity approach axisymmetry more closely after the first relaxation (at $t = 1.25$).

The core of the κ distribution is initially surrounded by a 'skirt' of low amplitude vorticity. Particularly, inside the regions $\mathscr{R}_1$ and $\mathscr{R}_2$, (note the humps on the contour $\kappa = 4$). This skirt of potential vorticity gives rise to the characteristic broad filaments seen at $t = 0.5$ through the convection in the corotating frame. In the meantime the stream function changes only a little, therefore the ω field also exhibits the broad filaments. During this time, remote particles in $\mathscr{R}_1$ and $\mathscr{R}_2$ with low amplitude κ are convected towards the core. Since the stream function changes little during this process, then negative values of ω are generated near the core (see figure 15 column one at $t = 0.75$).

It is crucial to observe that the streamlines are nearly elliptical and have a small aspect ratio. Hence the asymmetric part of the κ-field consists mainly of ω and the generation of negative ω becomes important in the axisymmetrization process. In order to calculate the orientation of the streamlines we may as a first approximation replace κ by ω in (26).

At early times the filaments and the negative ω-regions both contribute to a positive ϕ_d causing the first relaxation towards axisymmetry. At $t = 1.25$ the filaments have nearly the same symmetry as the elliptically symmetric core and the relaxation stops. At the same time the particles in $\mathscr{R}_1$ with the smaller κ (corresponding to the negative vorticity) have passed A_2 and are approaching A_1, thereby

giving an increasing contribution to a negative ϕ_d. The convection of these particles close to core contributes to the rapid increase in λ after $t = 1.25$. The filaments also contribute to a negative ϕ_d as they slowly move out of their symmetrical position. After $t = 1.25$, we observe λ_κ increases while the aspect ratio of the streamlines is still decreasing. This causes the negative ω to be intensified near the middle of the inner separatrices.

Eventually, the negative ω appears in the filaments and it becomes difficult to distinguish the net asymmetry. The positive and negative relative vorticity is almost uniformly distributed around the core at $t = 3.0$ resulting in a slow variation of λ_κ. At $t = 4.5$ the core has elongated to $\lambda_\kappa = 1.2$ and the convection in the ghost vortices again becomes significant.

6. Conclusion

In this paper we have demonstrated that an isolated near-elliptical smooth vorticity distribution relaxes to axisymmetry on a circulation timescale as the result of an inviscid mechanism. We have stated this mechanism in an axisymmetrization principle (13). The breaking of the elliptical symmetry of the vorticity field drives the axisymmetrization. The evolution of the asymmetric vorticity field produces filaments and gradient intensification in the core and is explained in terms of streamlines in a corotating frame.

The filaments have a dominant influence on the evolution of the vortex core, even when there is little circulation in the filaments. The reason is that only the asymmetric part of the vorticity field can deform the core and the filaments furnish most of the asymmetry. Note dissipative processes affect the vorticity amplitude in the filaments. However, their position and circulation are nearly unaffected.

On the basis of the axisymmetrization results it seems reasonable to conjecture that all isolated stable singly-connected, spatially-smooth steady-state solutions of the Euler equations are nearly axisymmetric.

From summer 1983, when the authors were at the National Center for Atmospheric Research (NCAR), the work was supported through National Science Foundation grants to NCAR. During the following period the work of M. V. Melander and N. J. Zabusky was supported by grants from the US Army Research Office, Mathematical Sciences Division (contract DAAG 29-84-K-0149) and the Office of Naval Research, code 422.PO (contract NOOOO 14-85-K-0024). All computations were made on the CRAY-1 computer at NCAR.

Appendix

Consider a vorticity field $\omega(x, y)$ periodic in the x- and y-directions with period 2π. Let $\omega(x, y)$ evolve according to

$$\partial_t \omega = [\nu_2 \Delta - \psi_4 \Delta^2]\omega - u\,\partial_x \omega - v\,\partial_y \omega, \tag{A 1}$$

where

$$(u, v) = (\partial_y, -\partial_x) \int_0^{2\pi} \int_0^{2\pi} \omega(\xi, \eta)\, G(x, y; \xi, \eta)\, \mathrm{d}\xi\, \mathrm{d}\eta, \tag{A 2}$$

and G is the doubly periodic Green function for Laplace's equation in $[0, 2\pi] \times [0, 2\pi]$.

In complex notation $z = x + \mathrm{i}y, \zeta = \xi + \mathrm{i}\eta$ we have

$$G(z, \zeta) = \frac{1}{2\pi} \sum_{n,\, m=-\infty}^{\infty} \ln |z - \zeta - 2\pi(n + \mathrm{i}m)|. \tag{A 3}$$

Assume that we add a uniform background ω_b to the vorticity field. This can only affect the evolution of $\omega(x,y)$ through the velocity field (u,v). The background contribution is

$$(u_b, v_b) = (\partial_y, -\partial_x) \int_0^{2\pi} \int_0^{2\pi} \omega_b G(x,y;\xi,\eta)\,\mathrm{d}\xi\,\mathrm{d}\eta$$
$$= \omega_b \int_0^{2\pi} \int_0^{2\pi} (\partial_\eta, -\partial_\xi) G(x,y;\xi,\eta)\,\mathrm{d}\xi\,\mathrm{d}\eta. \tag{A 4}$$

Using Green's theorem we find

$$u_b = -\omega_b \left[\int_0^{2\pi} G(x,y;\xi,0)\,\mathrm{d}\xi + \int_{2\pi}^{0} G(x,y;\xi,2\pi)\,\mathrm{d}\xi \right] = 0, \tag{A 5}$$

due to the periodicity of G. Similarly we find $v_b = 0$. Hence the background vorticity in the pseudospectral model has no influence on the evolution of the physical quantities.

REFERENCES

HAIDVOGEL, D. B. 1985 Particle dispersion and Lagrangian vorticity conservation in models of β-turbulence. *J. Phys. Oceanogr.* submitted.

HERNAN, M. A. & JIMENEZ, J. 1982 Computer analysis of a high speed film of the plane turbulent mixing layer. *J. Fluid Mech.* **119**, 323–345.

KIDA, S. 1981 Motion of an elliptic vortex in a uniform shear flow. *J. Phys. Soc. Japan* **50**, 3517–3520.

LAMB, H. 1932 *Hydrodynamics*, 6th edn, Cambridge University Press.

MCWILLIAMS, J. C. 1984 The emergence of isolated vortices in turbulent flow. *J. Fluid Mech.* **146**, 21–43.

MELANDER, M. V., STYCZEK, A. S. & ZABUSKY, N. J. 1984 Elliptically desingularized vortex model of the 2D Euler equations. *Phys. Rev. Lett.* **53**, 1222–1225.

MELANDER, M. V., ZABUSKY, N. J. & STYCZEK, A. S. 1986 A moment model for vortex interactions of the two-dimensional Euler equations. I. Computational validation of a Hamiltonian elliptical representation. *J. Fluid Mech.* **167**, 95–115.

OVERMAN, E. A. & ZABUSKY, N. J. 1982 Evolution and merger of isolated vortex structures. *Phys. Fluids* **25**, 1297–1305.

OVERMAN, E. A. & ZABUSKY, N. J. 1984 Diagnostic algorithms for contour dynamics. *Trans. First Army Conf. on Appl. Maths and Computing. ARO Rep.* 84-1, pp. 269–287.

PERRY, A. E., CHONG, M. S. & LIM, T. T. 1982 The vortex-shedding process behind two-dimensional bluff bodies. *J. Fluid Mech.* **116**, 77–90.

ZABUSKY, N. J. 1982 Computational synergetics and mathematical innovation. *J. Comp. Phys.* **195**.

ZABUSKY, N. J. 1984 Computational Synergetics. *Phys. Today*, July, 1–11.

ZABUSKY, N. J., HUGHES, M. H. & ROBERTS, K. V. 1979 Contour dynamics for the Euler equations in two dimensions. *J. Comp. Phys.* **30**, 96–106.